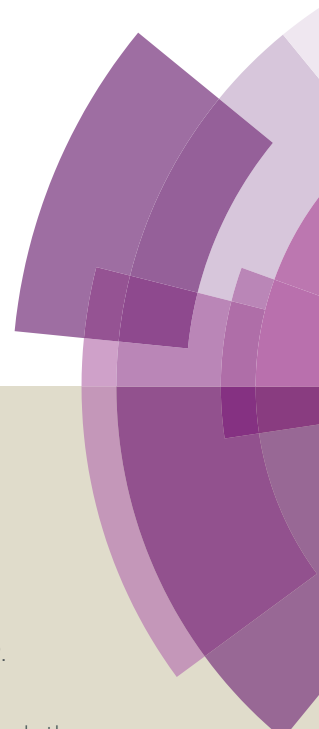


Journal of Materials Chemistry A

Accepted Manuscript



This article can be cited before page numbers have been issued, to do this please use: W. Luo, T. Liu, P. Zhao, X. Hua, S. Chen and G. Cheng, *J. Mater. Chem. A*, 2016, DOI: 10.1039/C6TA03265F.



This is an *Accepted Manuscript*, which has been through the Royal Society of Chemistry peer review process and has been accepted for publication.

Accepted Manuscripts are published online shortly after acceptance, before technical editing, formatting and proof reading. Using this free service, authors can make their results available to the community, in citable form, before we publish the edited article. We will replace this *Accepted Manuscript* with the edited and formatted *Advance Article* as soon as it is available.

You can find more information about *Accepted Manuscripts* in the [Information for Authors](#).

Please note that technical editing may introduce minor changes to the text and/or graphics, which may alter content. The journal's standard [Terms & Conditions](#) and the [Ethical guidelines](#) still apply. In no event shall the Royal Society of Chemistry be held responsible for any errors or omissions in this *Accepted Manuscript* or any consequences arising from the use of any information it contains.

Journal Name

ARTICLE

A Fe-N-C hybrid electrocatalyst derived from bimetal-organic framework for efficient oxygen reduction

Teng Liu, Pingping Zhao, Xing Hua, Wei Luo,* Shengli Chen* and Gongzhen Cheng

[†]Received 00th January 20xx,
Accepted 00th January 20xx

DOI: 10.1039/x0xx00000x

www.rsc.org/

A simple Zn/Fe bimetallic zeolitic-imidazole frameworks (ZIF) carbonization method is developed to synthesize a Fe-N-C hybrid with hierarchical nitrogen-doped porous carbons crossed by carbon nanotubes. Both the specific ratios of Zn/Fe in bimetallic metal-organic framework (MOF) precursors and the selected annealing temperature are essential for the formation of this unique hybrid structure with good conductivity and more active sites exposure. The resulted FeNC-20-1000 hybrid electrocatalyst exhibits excellent oxygen reduction reaction (ORR) activity, with a half-wave potential of 0.770 V comparable to that of commercial Pt/C catalysts in acidic media, and a half-wave potential of 0.880 V, ca. 50 mV more positive than Pt/C for ORR in alkaline solution. More importantly, the as-prepared Fe-N-C hybrid exhibits much more stability for the ORR in both acidic and alkaline solutions than those of Pt/C, which makes it among the best non-noble-metal catalysts ever reported for ORR under acidic and alkaline conditions.

Introduction

Electrochemical oxygen reduction reaction (ORR) is the key process in a wide range of the renewable energy technologies, such as fuel cells, and metal-air batteries.¹⁻³ Due to the sluggish reaction kinetics, to date, Pt-based materials are still the state-of-the-art catalysts.⁴⁻⁶ However, the scarce reserve, high cost, poor durability, and low poison resistance significantly prohibit their large-scale commercial application.^{7,8} Thus, great efforts have been made to develop low-cost, highly active and durable Pt-free electrocatalysts,⁹ including alloys,¹⁰⁻¹² metal oxides,^{8, 13, 14} and heteroatom-doped carbons.¹⁵⁻¹⁷ Among them, Fe-N decorated carbons (Fe-N-C) have been considered as promising candidates because of their low cost, comparable catalytic activity and durability.¹⁸⁻²⁰ Despite the great efforts in significantly enhancing ORR activity, most of their performances still can hardly match those of Pt especially in acid media.²¹⁻²³ It has been reported that a good balance between high specific surface area, hierarchical porosity, and high conductivity could result in a much faster mass transfer and more reactive sites exposure during the catalytic process, and thus boosting their ORR performances.^{24,25} In this regards, exploring more effective method to fabricate Fe-N decorated carbons with both desirable hierarchical porosity and conductivity may be the key to obtain highly active and stable nonprecious catalysts for ORR in both acidic and alkaline conditions, but it is still a great challenge.

On the other, metal-organic frameworks (MOFs) with large specific surface area, diverse structure, and large pore volume, have been widely studied as precursors and template for synthesizing hierarchical porous carbons for electrocatalytic ORR after carbonization.²⁶⁻²⁸ Very recently, the researchers found that using bimetallic MOFs as the precursors could increase surface area of the obtained carbons, and thus enhance ORR catalytic activity.^{29,30} However, the morphologies of these bimetallic MOFs are maintained well even after carbonization, which could result in low degree of graphitization and less reactive sites exposure. Therefore, conductive carbon materials, such as graphene and carbon nanotubes (CNTs), have been introduced during the synthesis of MOFs to increase the conductivity after carbonization, and thus further increase the catalytic performance.^{31,32}

By taking the advantage of *in situ* formation CNTs outside the hierarchical porous carbon,³³ herein, we reported a very simple method for manufacturing a Fe-N-C hybrid through annealing Zn and Fe bimetallic MOFs. As illustrated in Scheme 1, the introduction of Fe species could not only expose sufficient active sites,³⁴⁻³⁶ but also catalyzed the *in situ* formation of CNTs during the pyrolysis,³⁷ which may facilitate the mass transfer during the catalytic process. Thanks to the synergistic effect between the *in situ* formed nitrogen doped CNTs and hierarchical porous carbons, the Fe-N-C hybrid FeNC-20-1000 derived from carbonized bimetallic Zn/Fe-ZIF-20, exhibits an outstanding ORR activity with half-wave potential of 0.770 V, which is comparable to that of Pt/C catalyst 0.827 V in acidic solution. In particular, the half-wave potential is 0.880 V, ca. 50 mV more positive than Pt/C for ORR in alkaline solution.

College of Chemistry and Molecular Sciences, Wuhan University, Wuhan, Hubei 430072, P. R. China. Tel.: +86 2768752366. E-mail address: wluo@whu.edu.cn; slchen@whu.edu.cn

[†]Electronic Supplementary Information (ESI) available. See DOI: 10.1039/x0xx00000x

Experimental Section

Materials

Zinc nitrate hexahydrate ($\text{Zn}(\text{NO}_3)_2 \cdot 6\text{H}_2\text{O}$, Sinopharm Chemical Reagent Co., Ltd., 99%), Iron (II) sulfate heptahydrate ($\text{FeSO}_4 \cdot 7\text{H}_2\text{O}$, Sinopharm Chemical Reagent Co., Ltd., 99%), Potassium hydroxide (KOH, Sinopharm Chemical Reagent Co., Ltd., > 98%), Potassium chloride (KCl, Sinopharm Chemical Reagent Co., Ltd., 99%), Benzimidazole ($\text{C}_7\text{H}_6\text{N}_2$, Aladdin Reagent Co., Ltd., > 98%), Perchloric acid (HClO_4 , Sinopharm Chemical Reagent Co., Ltd., 70%-72%), N, N-dimethylformamide ($\text{C}_3\text{H}_7\text{NO}$, Sinopharm Chemical Reagent Co., Ltd., > 99.5%), methanol (CH_3OH , Sinopharm Chemical Reagent Co., Ltd., > 99.8%), nafion® perfluorinated resin solution ($\text{C}_9\text{HF}_{17}\text{O}_5\text{S}$, Sigma Aldrich Co., 5 wt.% in lower aliphatic alcohols and water), Carbon-supported platinum (Pt/C, Hesen electric Co., Ltd., 20%), ultrapure water (used as the reaction solvent).

Preparation of ZIF-7

The synthesis of ZIF-7 was according to the literature with some modifications.³⁸ $\text{Zn}(\text{NO}_3)_2 \cdot 6\text{H}_2\text{O}$ (0.744 g, 2.5 mmol) and c(1.18 g, 10 mmol) was dissolved in 60 mL DMF in a 100 mL vial, then it was heated to 130 °C at a rate of 5 °C /min and held at this temperature for 24 h. After natural cooling, ZIF-7 crystals were scraped from the inner surface of the vial, separated by centrifugation, washed with methanol several times and dried under reduced pressure at room temperature.

Preparation of Zn/Fe-ZIF-X

The synthesis procedure of Zn/Fe-ZIF-X (X means the molar ratio between Zn^{2+} and Fe^{2+} in the precursor) was similar to ZIF-7. $\text{Zn}(\text{NO}_3)_2 \cdot 6\text{H}_2\text{O}$ and $\text{FeSO}_4 \cdot 7\text{H}_2\text{O}$ was dissolved in DMF with different molar ratio of $\text{Zn}^{2+}/\text{Fe}^{2+}$, then benzimidazole was added to the solution with 4 times the amount of the metal ion. The rest of the synthesis process was the same as that of ZIF-7 mentioned above.

Preparation of FeNC-X-1000 and FeNC-20-Y

FeNC-X-1000 was obtained by means of a simple one-step pyrolysis method. In a typical process, 500 mg Zn/Fe-ZIF-X was heated to 1000 °C at a rate of 5 °C /min in the tube-furnace under a N_2 flow and maintained at this temperature for 1 hour. Then it was gradually cooled to the room temperature, washed with 0.5 M H_2SO_4 for 12 h at room temperature and dried by cryodesiccation. The synthesis of FeNC-20-Y (Y means the pyrolysis temperature) was similar to FeNC-20-1000 except that the pyrolysis temperature changed.

Characterization

Powder X-ray diffraction (XRD) patterns were measured by a Bruker D8-Advance X-ray diffractometer with $\text{CuK}\alpha$ radiation source ($\lambda = 0.154178$ nm). Raman spectroscopy was performed with a laser micro-Raman spectrometer (Renishaw in Via, 532 nm excitation wavelength). X-ray photoelectron spectroscopy (XPS) measurement was achieved with a Thermo Fischer ESCALAB 250Xi spectrophotometer. The inductively coupled plasma atomic emission spectroscopy (ICP-AES) was detected on IRIS Intrepid II XSP (Thermo Fisher Scientific, USA). The Brunauer-Emmett-Teller (BET) surface area was collected by N_2 adsorption using a

Quantachrome NOVA 4200e. The SEM images were obtained with a Zeiss Sigma scanning electron microscope. The TEM images were observed by using a Tecnai G20 U-Twin transmission electron microscope equipped with an energy dispersive X-ray detector (EDX).

Electrochemical measurements

The catalysts' ORR efficiency was evaluated on a CHI 760E workstation in both alkaline and acidic media. The RDE measurement of the all catalysts was achieved on the surface of a glassy carbon rotating disk electrode (GC RDE) and the RRDE performance was carried out with a glassy carbon rotating ring-disk electrode (GC RRDE), both of which had been polished using 0.05 μm alumina slurry and washed with ultrapure water. Counter electrode was a platinum foil. Hg/HgO electrode soaked in 0.1 M KOH and Hg/HgCl electrode soaked in saturated KCl solution were used as the reference electrode in alkaline media and acid media respectively. All the electrochemical tests were performed at room temperature.

The catalytic ink was prepared in a small glass bottle, 5 mg sample was added to 1 mL isopropanol solvent containing 0.1% Nafion and then ultrasound-treated for half an hour. For FeNC-X-Y (X refers to the molar ratio between Zn^{2+} and Fe^{2+} in the precursor, Y refers to the pyrolysis temperature) catalysts, 30 μL ink suspension was deposited on the surface of a GC RDE with a surface area of about 0.1964 cm^2 (for RDE test) or 38.4 μL ink on a GC RRDE with a surface area of 0.2475 cm^2 (for RRDE test) and dried naturally.

The solutions had been saturated by high-purity O_2 or N_2 for half an hour before each experiment and a flow of O_2 or N_2 was maintained during the measurements. The working electrode was activated at a scanning rate of 500 mV s^{-1} for several cycles. To obtain the CV of RDE and RRDE in both O_2 or N_2 , the negative-direction sweep of potential was from 1.10 V to 0.10 V at a rate of 5 mV s^{-1} with the electrode speed of 1600 rpm in 0.1 M KOH solution, and from 1.00 V to 0.20 V with the same scan rate and electrode speed in 0.1 M HClO_4 solution. For the stability tests, the initial potential was set at -0.16 V in 0.1 M KOH or 0.36 V in 0.1 M HClO_4 respectively.

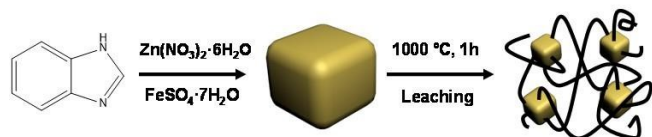
The potential was converted to the potential versus reversible hydrogen electrode (RHE). Firstly, the media was saturated with H_2 by the inrush of hydrogen for half an hour, a GC RDE coated with 6 μL Pt/C was used as the working electrode, then the hydrogen electrode reactions (HERs) were carried out at a scan rate of 5 mV s^{-1} to obtain the polarization curve, the potential at which current crossed zero was chosen as the RHE zero potential. Koutecky-Levich plots (J^{-1} vs. $\omega^{-1/2}$) were analysed at 0.5, 0.6, 0.7, 0.8 V in 0.1 M KOH and 0.4, 0.5, 0.6, 0.7 V in 0.1 M HClO_4 with varying rotating speed. The electron transfer number (n) was calculated on the Koutecky-Levich equation:¹⁴

$$\frac{1}{J} = \frac{1}{J_L} + \frac{1}{J_K} = \frac{1}{B\omega^{1/2}} + \frac{1}{J_K}$$

$$B = 0.62nFC_o(D_o)^{2/3}\nu^{-1/6} \quad J_K = nFkC_o$$

where J means the measured current density, J_K and J_L are the kinetic- and diffusion-limiting current densities respectively, ω means the angular velocity, n means the electron transfer number, F means the Faraday constant, C_0 is the bulk concentration of O_2 , ν means the kinematic viscosity of the electrolyte, and k means the electron-transfer rate constant.

Results and discussion



Scheme 1 Schematic illustration of the synthetic process of the FeNC-20-1000.

In order to design the Zn/Fe bimetallic MOFs, a method similar to the synthesis of ZIF-7 was introduced, in which both $Zn(NO_3)_2 \cdot 6H_2O$ and $FeSO_4 \cdot 7H_2O$ were added through a one-pot method. The bimetallic MOFs named Zn/Fe-ZIF-X were control synthesized by modulating the initial Zn^{2+}/Fe^{2+} ratio of the precursors. In the Powder X-ray diffraction (PXRD) pattern of the obtained Zn/Fe-ZIF-X materials, a series peaks similar to ZIF-7 were observed, indicating their high crystallinities and similar zeolite-type structures (Fig. S1, Supporting Information). Furthermore, as the molar ratio of Zn/Fe decrease, the color of the as-synthesized Zn/Fe-ZIFs gradually changed from white to reddish-brown, indicating that Fe^{2+} ions were successfully doped into ZIF-7 to form the uniform Zn/Fe-ZIFs

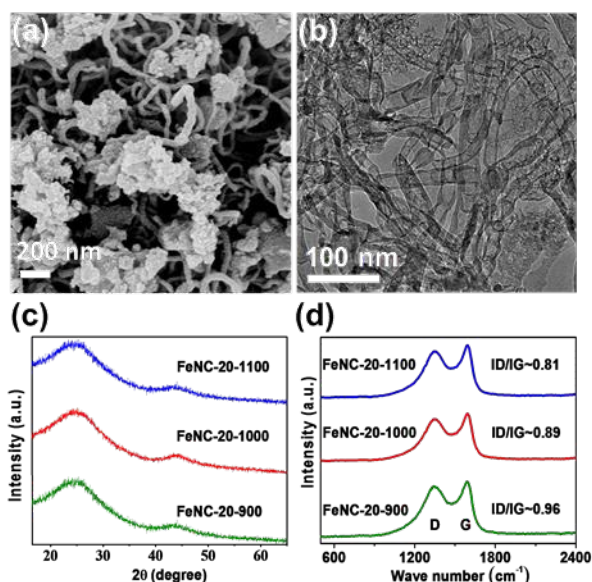


Figure 1 Electron microscopy characterization of FeNC-20-1000 (a) SEM image, (b) TEM image. XRD patterns (c) and Raman spectra (d) of FeNC-20-900, FeNC-20-1000, FeNC-20-1100.

(Fig. S2).^{29, 39} The SEM images show that the size and shape of the bimetallic Zn/Fe-ZIFs were highly dependent on the metallic component, while the polyhedral shaped nanocrystals decreased gradually as the Zn/Fe molar ratios decreased (Fig. S3). Taking one representative Zn/Fe-ZIF-20 as example, the uniform distribution of Zn and Fe in the bimetallic MOFs was further confirmed by elemental mapping, as shown in Fig. S4. The Zn/Fe-ZIF-20 was further pyrolyzed at 1000 °C for 1 h in the furnace under a N_2 flow. After leaching by 0.5 M H_2SO_4 for 12 h to remove the unstable metal species, the FeNC-20-1000 was obtained (in FeNC-X-Y, X means the molar ratio between Zn and Fe in the precursor, Y means the annealed temperature).

The morphologies of obtained Fe-N-C catalysts were investigated by scanning electron microscopy (SEM) and transmission electron microscopy (TEM). The SEM image showed a hybrid structure of N-doped CNTs and porous carbon in Fig. 1a. Large amount of CNTs clusters were observed crossing the porous carbons, interlinking them into a 3D network. The average diameter of the CNTs is about 30 nm, which is in the typical range of mesoporous size. Such special structure of porous carbon crossed by CNTs, could make FeNC-20-1000 catalyst achieve an enhanced electrochemical performance due to the large amount of active sites exposure and the fast mass transfer. The elemental mapping analysis of FeNC-20-1000 further confirmed the uniform distribution of C, N and Fe (Fig. S5). The TEM image was shown in Fig. 1b, a hybrid of porous carbon nanosheets crossed by a large number of carbon nanotubes was observed, with no clear metallic nanoparticles. For comparison, Zn/Fe-ZIF-20 annealed at 900 °C and 1100 °C, and the obtained FeNC-20-900 and FeNC-20-1100 were also characterized by SEM and TEM (Fig. S6). Both FeNC-20-900 and FeNC-20-1100 exhibited the formation of aggregated porous carbon, without significant change to the polyhedral shape nanocrystals compared to their Zn/Fe-ZIF-20 precursors. These results indicated that an appropriate annealed temperature is essential for the synthesis of the desired hybrid structure with porous carbon crossed by CNTs. To capture the formation of CNT, we set the remaining time of the target temperature (1000 °C) at 0 min to get the sample FeNC-20-1000-0. Once the temperature reached 1000 °C, the calcined program was began to cool down. We found that large amount of CNTs formed in FeNC-20-1000-0, indicating that CNTs may be formed in the elevating temperature stage (only 20 min) from 900 to 1000 °C (Fig. S7a). Combining the fact that no CNTs forming at 900 °C, this result implied that CNTs could be formed in a very short time. To demonstrate the role of MOFs, we use a mixture of benzimidazole, $Zn(NO_3)_2 \cdot 6H_2O$ and $FeSO_4 \cdot 7H_2O$ as the precursors to get FeNC-20-1000-con, under the same program as FeNC-20-1000. As shown in Fig. S7b, only large carbon layers without the formation of CNT were obtained. The reason that ZIF resulting in the formation of CNTs may be due to its unique structure with a uniform distribution of iron species, and the strong interaction between Fe species and organic ligands (carbon sources). Carbon nanoshells with Fe-based species encapsulated were suggested to be the key fact to catalyze the formation of CNT, based on recent results reported by several groups.^{33,39,41}

X-ray diffraction (XRD) and Raman spectroscopic measurements were used to investigate the physical information of the as-

obtained catalysts (Fig. 1c). The typical peaks at around 26° and 44° , could be assigned to the lattice plane of (002) and (101) of graphite carbon respectively. No obvious diffraction peak of Zn and Fe phases could be observed. Most of Zn species could be evaporated during the high-temperature pyrolyzation, and Fe species were most likely removed during the acid leaching process, or incorporated into carbons with amorphous form, which is agree well with TEM analysis. Inductively coupled plasma emission spectroscopy (ICP-AES) was used to measure the content of iron. As a result, there are only 0.73 wt%, 0.49 wt% and 2.2 wt% of Fe in FeNC-20-900, FeNC-20-1000, and FeNC-20-1100 respectively. As shown in Fig. 1d, G (1590 cm^{-1}) and D (1345 cm^{-1}) bands were detected by Raman spectroscopy to identify the information of defective and graphitization. Among the three samples tested, FeNC-20-1000 reached a balance between large amount of defective sites and high graphitization with an ID/IG value of 0.89, which is conducive to acquire a good conductivity and exposure more active sites.

X-ray photoelectron spectroscopy (XPS) measurements were carried out to further investigate the chemical compositions and surface information of the catalysts. The high-resolution N 1s spectra of FeNC-20-1000 were deconvoluted into four different peaks, 398.3, 399.8, 401.0 and 402.7 eV, corresponding to pyridinic N, pyrrolic N, graphitic N and oxidized N, respectively, as shown in Fig. S8b. For comparison, the XPS of FeNC-20-900 and FeNC-20-1100 were also studied (Fig. S8a, c). The amount of pyridinic N and pyrrolic N decreased while the content of graphitic N and oxidized N increased with the pyrolysis temperature increased (Fig. S9). However, in the Fe 2p range, as shown in Fig. S10, the Fe species were hardly to analyze due to the low content of iron, which was in agreement with the XRD and TEM results. Very recently, pyridine N was demonstrated to be the major reason to enhance the performance of ORR from DFT method and experimental data in N/C materials.^{42,43} The electron density of C atoms close to pyridine N was strongly decreased and thus acted as ORR active centers.⁴⁴ Fe-Nx with a planar structure or C atoms surrounded Fe-Nx planar was also thought to be the active sites for ORR.⁴⁵⁻⁴⁷ Therefore, a combination of N/C and transition metal (Fe) was suggested to be responsible for the superior ORR activity in our Fe-N-C systems.⁴⁸

N_2 adsorption/desorption method was used to measure the surface area and the porous property of FeNC-20-1000, as shown in Fig. S11b. A typical type-IV isotherm was observed, indicating the mesoporous structure. From the DFT pore size distribution (Fig. S11e), a wide range spanned from micropores to mesopores was observed, demonstrated the hierarchical architecture of the as-synthesized catalyst, which is essential for the fast mass transfer during the catalytic process toward ORR.^{49,50} For comparisons, the FeNC-20-900 and FeNC-20-1100 samples were also characterized by N_2 adsorption-desorption, showed in Fig. S11a, c, d, f.

The electrocatalytic activity of the as-obtained FeNC catalysts toward ORR in 0.1 M KOH solution was compared with the

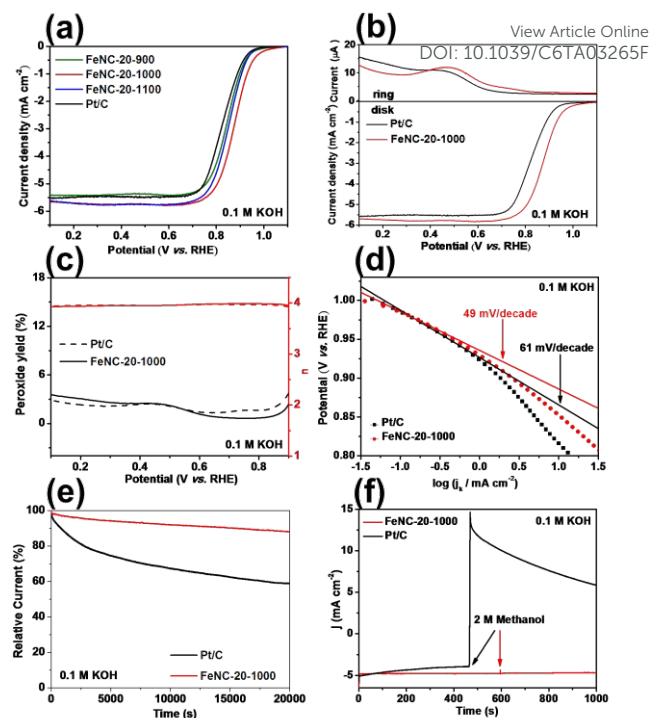


Figure 2 (a) LSV curve of FeNC-20-900, FeNC-20-1000, FeNC-20-1100 and Pt/C in 0.1 M KOH. (b) RRDE voltammograms of FeNC-20-1000 (red) and Pt/C (black) in 0.1 M KOH. (c) Percentage of peroxide (black) and the electron transfer number (n) (red) of FeNC-20-1000 (solid line) and Pt/C (dotted line). (d) The corresponding Tafel slope of FeNC-20-1000 (red) and Pt/C (black). (e) Current-time curves of FeNC-20-1000 (red) and Pt/C (black), the currents were converted to current percentage. (f) Chronoamperometric responses to addition of 2 M methanol. The experiments mentioned above performed with the rotating speed of 1600 rpm and the scan rate of 5 mV s^{-1} . All the catalyst loading was 0.75 mg cm^{-2} except for Pt/C (0.15 mg cm^{-2}).

commercial 20 wt% Pt/C using the rotating ring-disk electrode (RDE) and rotating ring-disk electrode (RRDE) techniques. The CV curve in both O_2 and N_2 saturated solution was shown in Fig. S14a. The current-potential responses in ORR range, as shown in Fig. 2, have been subtracted from those under N_2 . Among all the three FeNC samples, the hybrid FeNC-20-1000 exhibits the highest catalytic activity, with the onset potential of 1.04 V, 70 mV higher than that of Pt/C (0.97 V); half-wave potential ($E_{1/2}$) of 0.88 V, 50 mV higher than that of Pt/C. In the range of testing, the corresponding H_2O_2 yield of FeNC-20-1000 catalyst was lower than 4% (Fig. 2c). According to the relevant work, the reaction pathway during ORR catalyzed by Pt/C or Fe-N-C catalysts were highly dependent on its loading.^{51,52} To test the reaction pathway during catalytic process, we investigated the steady-state current-potential responses using RDE technology with different catalyst loading. The corresponding Koutecky-Levich plots exhibited that the electron transfer numbers were calculated to be 2.51, 3.92, 3.99, and 3.99 for the catalysis loading of 0.03, 0.15, 0.45 and 0.75 mg cm^{-2} , respectively (Fig. S15). The apparent four-electron pathway catalyzed at high loading range originated from the re-reduction of H_2O_2 produced inside the

electrode. And such long range diffusion path was responsible for the negligible apparent H_2O_2 content tested by the electrolyte. Thus, in RRDE test, we believed that the apparent H_2O_2 detected by ring electrode and the corresponding electron transfer number was not the real nature catalyzed by the as-obtained Fe-N-C materials with a high loading. Tafel plots of FeNC-20-1000 was calculated to be 49 mV/dec, much lower than that of Pt/C (61 mV/dec), indicating a more desirable ORR kinetics occurred (Fig. 2d). Current-time curves were studied for the investigation of durability test, as shown in Fig. 2e. The relative current of FeNC-20-1000 catalyst remained 89% after 20,000s, much better than that of the commercial Pt/C (59%). Methanol tolerance test was carried out using chronoamperometric responses to methanol for both FeNC-20-1000 and Pt/C. 2 M MeOH was added into the system at the point of 400 s during the i-t test, an obvious change occurred in the ORR current for Pt/C as a result of methanol oxidation reaction. While the current recovered quickly after a transitory disturbance for FeNC-20-1000, indicating an excellent methanol resistance ability. To the best of our knowledge, the outstanding performance toward ORR makes the as-obtained FeNC-20-1000 catalyst surpassed most of the non-precious metal-based catalysts reported previously in alkaline media, as listed in Table S1.

Furthermore, the catalytic performance of FeNC samples were also investigated in acid media measured by RDE and RRDE methods, a similar situation occurs in 0.1 M HClO_4 , the FeNC-20-1000 catalyst still exhibited the highest catalytic activity. The CV curve in both O_2 and N_2 saturated solution was shown in Fig. S14b, the polarization curves obtained in N_2 have been deduced from the polarization curves obtained in O_2 . As shown in Fig. 3a, the E_{on} and $E_{1/2}$ of FeNC-20-1000 are 0.90 and 0.770 V, which are only 70 and 57 mV negatively shifted compared to that of Pt/C, higher than most of the reported results (Table S2, Supporting Information). The H_2O_2 yield was lower than 2% for FeNC-20-1000, and the apparent electron transfer number was 3.99 (Fig. 3b, c). In the Koutecky-Levich plots resulted from the RDE voltammograms (Fig. S16), the electron transfer numbers were calculated to be 3.25, 3.92, and 3.97 for the catalysis loading of 0.15, 0.45, and 0.75 mg cm^{-2} , respectively. H_2O_2 molecules were hindered by the thick layers during its diffusion to ring electrode, which would lead to a lower apparent H_2O_2 content and a larger electron transfer number in RRDE test.⁴⁹ Tafel plots of FeNC-20-1000 and Pt/C catalyst are almost the same, which indicates a similar kinetic process between FeNC-20-1000 and Pt/C (Fig. 3d). The chronoamperometric approach was also used to identify the durability and the methanol tolerance of FeNC-20-1000 and Pt/C in 0.1 M HClO_4 . As a result, the relative current of FeNC-20-1000 catalyst remained 75% after 20,000s of continuous operation, while only 7.5% was left for Pt/C in the same condition (Fig. 3e). In the test of methanol tolerance, no obvious impact appeared on the current of FeNC-20-1000 as 2 M methanol added into the system during i-t experiment, while the current of Pt/C showed an instantaneous jump due to the cross effect of methanol oxidation reaction (Fig. 3f).

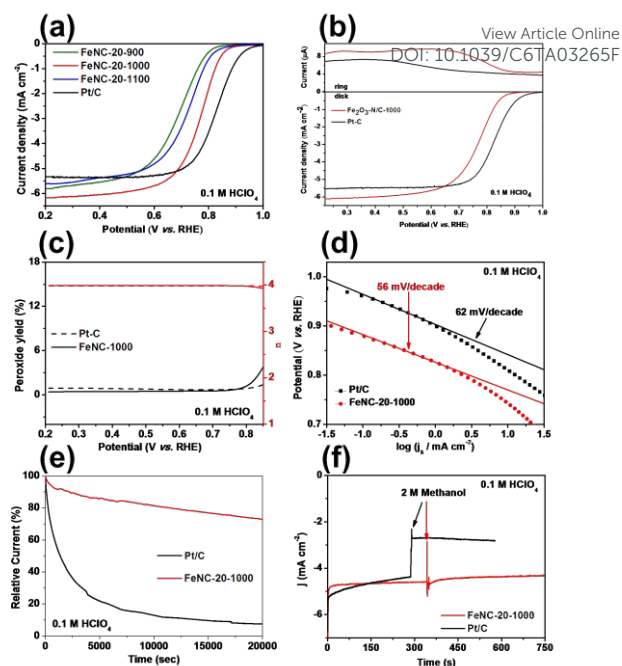


Figure 3 (a) LSV curve of FeNC-20-900, FeNC-20-1000, FeNC-20-1100 and Pt/C in 0.1 M HClO_4 . (b) RRDE voltammograms of FeNC-20-1100 (red) and Pt/C (black) in 0.1 M HClO_4 . (c) Percentage of peroxide (black) and the electron transfer number (n) (red) of FeNC-20-1000 (solid line) and Pt/C (dotted line). (d) The corresponding Tafel slope of FeNC-20-1000 (red) and Pt/C (black). (e) Current-time curves of FeNC-20-1000 (red) and Pt/C (black), the currents were converted to current percentage. (f) Chronoamperometric responses to addition of 2 M methanol. The experiments mentioned above performed with the rotating speed of 1600 rpm and the scan rate of 5 mV s^{-1} . All the catalyst loading was 0.75 mg cm^{-2} except for Pt/C (0.15 mg cm^{-2}).

The extraordinary electrochemical performance of FeNC-20-1000 towards ORR in both acid and alkaline solution might be caused by the synergistic effect between the nitrogen doped CNTs and nitrogen doped hierarchical porous carbons, which resulted in a balance of the outstanding conductivity, faster mass transfer and sufficient active sites exposure. To further investigate the influence of Zn/Fe ratios in the precursors, different bimetallic Zn/Fe-ZIFs were used as precursors to synthesize FeNC catalysts at 1000 °C, named FeNC-X-1000. There is no difference in the XRD patterns of these samples, however, a weak increase of ID/IG from Raman spectra, suggesting the defects of FeNC-X-1000 samples rising slightly with the decrease of X (Fig. S10). The morphologies of these samples were further characterized by SEM, as shown in Fig. S11, the amount of CNT increased with the increased content of iron. Without adding iron, the morphology of ZIF-7 was maintained well after carbonization, without the formation of CNT. However, large amount of iron would result in bulk carbons, while FeNC-20-1000 reached a balance of maintaining nanoscale porous carbon and sufficient CNTs. RDE was used for FeNC-X-1000 to further study their electrocatalytic activity towards ORR in both alkaline and acid media, shown in Fig. 4. A similar tendency can be observed both in alkaline and acid solution. Pure ZIF-7, after annealed at 1000

°C, named ZIF-7-1000, exhibits the lowest catalytic activity, indicating that the introduction of iron into the bimetallic MOFs precursors, can not only catalyze the in situ formation of CNTs, but also expose sufficient active sites. While X increased in the range from 1 to 20, both the onset potential and half-wave potential showed a positive shift. Further increasing X would lead to a negative shift relatively. As a result, FeNC-20-1000 exhibited the best performance among the FeNC-X-1000 samples. Thus, a proper ratio of Zn^{2+}/Fe^{2+} was essential for the synthesis of appropriate bimetallic Zn/Fe-ZIF precursors, which may affect the structure and morphology of FeNC catalysts, and further influence their electrocatalytic activity toward ORR. In addition, the ORR activity of FeNC-20-1000-com obtained from annealing mixture of benzimidazole, $Zn(NO_3)_2 \cdot 6H_2O$ and $FeSO_4 \cdot 7H_2O$ was studied. As shown in Fig. S17, a much lower activity than those of FeNC-20-1000 in both alkaline and acid solution were observed. These results indicated that the successful synthesis of the unique architecture as well as its outstanding electro-catalytic performance were highly related to ZIF with a stable and uniform distribution of Fe, N and C.

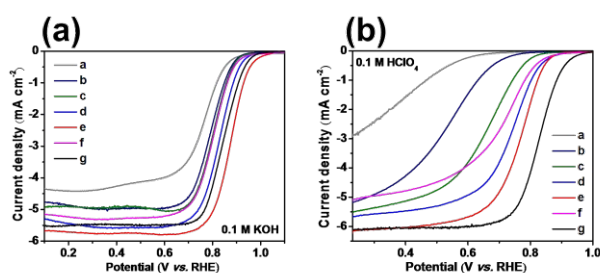


Figure 4 LSV curve of ZIF-7-1000 (a), FeNC-24-1000 (b), FeNC-20-1000 (c), FeNC-16-1000 (d), FeNC-8-1000 (e), FeNC-1-1000 (f) and Pt/C (g) in (a) 0.1 M KOH, (b) 0.1 M $HClO_4$. The experiments mentioned above performed with the rotating speed of 1600 rpm and the scan rate of 5 mV s^{-1} . All the catalyst loading was 0.75 mg cm^{-2} except for Pt/C (0.15 mg cm^{-2}).

Based on the previously reports, in both Pt/C and M-N-C system, the oxygen reduction reaction was highly dependent on the catalyst size, which is called 'particle size effect'. The appearance of two-electron or four-electron reduction pathway may be influenced at the same time.⁵³ Both the morphology of electrocatalysts and irrespective ORR kinetics influenced the fuel cell performance strongly. It is a big issue about the mass-transport process in such a multilayer cathodic environment, which is a pervasive problem encountered in Fe-N-C catalytic systems. The difficulty of oxygen molecules passing close to the active sites embedded inside and the final product leaving away from these active sites will lead to a lowered performance of fuel cell operation. On one hand, back pressure influence the penetrability of oxygen molecules toward the active sites. Generally speaking, larger back pressure will lead to a better mass-transport of oxygen toward the active sites in a certain range, which is different from the aqueous solution system with oxygen molecules saturated. On the other hand, water

molecules cannot diffuse into the bulk system through such a multilayer path smoothly, resulting in the block of these active sites. Flooding is easier to happen so that further oxygen molecules incoming would be hindered and the fuel cell performance was limited. Based on these analysis, IR losses originated from the preventing process of mass-transport also. Above all, two aspects should be considered in the actual fuel cell: (1) the transport of oxygen molecules to the active sites; and (2) the removal of water.^{54,55} Further work about enhancing the mass-transport efficiency of non-precious metal based system in the real fuel cell operation is still underway.

Conclusions

A series of FeNC catalysts derived from bimetallic Zn/Fe-ZIFs were prepared by a simple one-step pyrolysis method and showed extraordinary ORR performance in both alkaline and acid media. The key part of our synthesis is the introducing of iron into the ZIF-7 precursors to form bimetallic MOFs, which can not only catalyze the in situ formation of CNTs, but also expose sufficient active sites. We found the selected annealing temperature play the key role in the formation of the hybrid structure, while annealed at 900 and 1100 °C only resulted the porous carbons without the formation of CNTs. Thanks to the synergistic effect between the nitrogen doped CNTs and nitrogen doped hierarchical porous carbons in the hybrid, FeNC-20-1000 exhibited the highest catalytic performance among all the catalysts tested, with high ORR catalytic activity and stability in both alkaline and acid media, making it one of the best non-precious metal catalyst ever reported.^{56,57} Besides, this work may open an avenue for in situ constructing hybrids of nitrogen doped carbon nanotubes and porous carbon nanosheets from bimetallic MOFs for more applications.

Acknowledgements

This work was financially supported by the Ministry of Science and Technology of China under the National Basic Research Program (Grant nos. 2012CB215500 and 2012CB932800), National Natural Science Foundation of China (Grant nos. 21201134 and 21571145), the Natural Science Foundation of Jiangsu Province (BK20130370), the Creative Research Groups of Hubei Province (2014CFA007) and Large-scale Instrument and Equipment Sharing Foundation of Wuhan University.

References

1. K. Gong, F. Du, Z. Xia, M. Durstock and L. Dai, *Science*, 2009, **323**, 760-764.
2. S. Chen, Y. Liu and J. Chen, *Chem. Soc. Rev.*, 2014, **43**, 5372-5386.
3. M. Shao, Q. Chang, J.-P. Dodelet and R. Chenitz, *Chem. Rev.*, 2016, **116**, 3594-3657.

4. C.-J. Zhong, J. Luo, P. N. Njoki, D. Mott, B. Wanjala, R. Loukrakpam, S. Lim, L. Wang, B. Fang and Z. Xu, *Energy Environ. Sci.*, 2008, **1**, 454-466.
5. G. Wu and P. Zelenay, *Acc. Chem. Res.*, 2013, **46**, 1878-1889.
6. L. Dai, Y. Xue, L. Qu, H.-J. Choi and J.-B. Baek, *Chem. Rev.*, 2015, **115**, 4823-4892.
7. C. Sealy, *Mater. Today*, 2008, **11**, 65-68.
8. G. Wu, K. L. More, C. M. Johnston and P. Zelenay, *Science*, 2011, **332**, 443-447.
9. R. Bashyam and P. Zelenay, *Nature*, 2006, **443**, 63-66.
10. G. Nam, J. Park, M. Choi, P. Oh, S. Park, M. G. Kim, N. Park, J. Cho and J.-S. Lee, *ACS nano*, 2015, **9**, 6493-6501.
11. X. Fu, Y. Liu, X. Cao, J. Jin, Q. Liu and J. Zhang, *Appl. Catal. B: Environ.*, 2013, **130**, 143-151.
12. S. Li, L. Zhang, J. Kim, M. Pan, Z. Shi and J. Zhang, *Electrochim. Acta*, 2010, **55**, 7346-7353.
13. M. Sun, Y. Dong, G. Zhang, J. Qu and J. Li, *J. Mater. Chem. A*, 2014, **2**, 13635-13640.
14. Y. Liang, Y. Li, H. Wang, J. Zhou, J. Wang, T. Regier and H. Dai, *Nat. mater.*, 2011, **10**, 780-786.
15. C. H. Choi, S. H. Park and S. I. Woo, *Green Chem.*, 2011, **13**, 406-412.
16. H. Zhu, J. Yin, X. Wang, H. Wang and X. Yang, *Adv. Funct. Mater.*, 2013, **23**, 1305-1312.
17. Z. Zhao, M. Li, L. Zhang, L. Dai and Z. Xia, *Adv. Mater.*, 2015, **27**, 6834-6840.
18. Y. C. Wang, Y. J. Lai, L. Song, Z. Y. Zhou, J. G. Liu, Q. Wang, X. D. Yang, C. Chen, W. Shi and Y. P. Zheng, M. Rauf, S.-G. Sun, *Angew. Chem. Int. Ed.*, 2015, **127**, 10045-10048.
19. A. Serov, K. Artyushkova and P. Atanassov, *Adv. Energy Mater.*, 2014, **4**.
20. S. Zhang, H. Zhang, Q. Liu and S. Chen, *J. Mater. Chem. A*, 2013, **1**, 3302-3308.
21. L. Lai, J. R. Potts, D. Zhan, L. Wang, C. K. Poh, C. Tang, H. Gong, Z. Shen, J. Lin and R. S. Ruoff, *Energy Environ. Sci.*, 2012, **5**, 7936-7942.
22. R. Othman, A. L. Dicks and Z. Zhu, *Int. J. Hydrogen Energy*, 2012, **37**, 357-372.
23. L. Lin, Q. Zhu and A.-W. Xu, *J. Am. Chem. Soc.*, 2014, **136**, 11027-11033.
24. B. Zhang, L. Fan, H. Zhong, Y. Liu and S. Chen, *J. Am. Chem. Soc.*, 2013, **135**, 10073-10080.
25. D. Geng, N. Ding, T. S. Andy Hor, Z. Liu, X. Sun and Y. Zong, *J. Mater. Chem. A*, 2015, **3**, 1795-1810.
26. A. Kong, Q. Lin, C. Mao, X. Bu and P. Feng, *Chem. Commun.*, 2014, **50**, 15619-15622.
27. X. Wang, J. Zhou, H. Fu, W. Li, X. Fan, G. Xin, J. Zheng and X. Li, *J. Mater. Chem. A*, 2014, **2**, 14064-14070.
28. S. Zhao, H. Yin, L. Du, L. He, K. Zhao, L. Chang, G. Yin, H. Zhao, S. Liu and Z. Tang, *ACS nano*, 2014, **8**, 12660-12668.
29. Y. Z. Chen, C. Wang, Z. Y. Wu, Y. Xiong, Q. Xu, S. H. Yu and H. L. Jiang, *Adv. Mater.*, 2015, **27**, 5010-5016.
30. B. You, N. Jiang, M. Sheng, W. S. Drisdell, J. Yano and Y. Sun, *ACS Catal.*, 2015, **5**, 7068-7076.
31. P. Su, H. Xiao, J. Zhao, Y. Yao, Z. Shao, C. Li and Q. Yang, *Chem. Sci.*, 2013, **4**, 2941-2946.
32. J. Wei, Y. Hu, Y. Liang, B. Kong, J. Zhang, J. Song, Q. Bao, G. P. Simon, S. P. Jiang and H. Wang, *Adv. Funct. Mater.*, 2015, **25**, 5768-5777.
33. H. T. Chung, J. H. Won and P. Zelenay, *Nat. commun.*, 2013, **4**, 1922.
34. M.-Q. Wang, W.-H. Yang, H.-H. Wang, C. Chen, Z.-Y. Zhou and S.-G. Sun, *ACS Catal.*, 2014, **4**, 3928-3936. DOI: 10.1039/C4TA03265F
35. Q. Wang, Z.-Y. Zhou, Y.-J. Lai, Y. You, J.-G. Liu, X.-L. Wu, E. Terefe, C. Chen, L. Song and M. Rauf, N. Tian, S.-G. Sun, *J. Am. Chem. Soc.*, 2014, **136**, 10882-10885.
36. J.-S. Lee, G.U. Park, S.T. Kim, M. Liu and J. Cho, *Angew. Chem. Int. Ed.*, 2013, **52**, 1026-1030.
37. G. C.-K. Liu and J. Dahn, *Appl. Catal., A*, 2008, **347**, 43-49.
38. K. S. Park, Z. Ni, A. P. Côté, J. Y. Choi, R. Huang, F. J. Uribe-Romo, H. K. Chae, M. O'Keeffe and O. M. Yaghi, *Proc. Natl. Acad. Sci.*, 2006, **103**, 10186-10191.
39. X. Wang, H. Zhang, H. Lin, S. Gupta, C. Wang, Z. Tao, H. Fu, T. Wang, J. Zheng and G. Wu, *Nano Energy*, 2016, **25**, 110-119.
40. W. Yang, X. Liu, X. Yue, J. Jia and S. Guo, *J. Am. Chem. Soc.*, 2015, **4**, 1436-1439.
41. J. Zhu, M. Xiao, C. Liu, J. Ge, J. St-Pierre and W. Xing, *J. Mater. Chem. A*, 2015, **43**, 21451-21459.
42. D. Guo, R. Shibuya, C. Akiba, S. Saji, T. Kondo and J. Nakamura, *Science*, 2016, **351**, 361-365.
43. T. Xing, Y. Zheng, L. H. Li, B. C.C.Cowie, D. Gunzelmann, S. Z. Qiao, and Y. Chen, *ACS Nano*, 2014, **7**, 6856-6862.
44. C. V. Rao, C. R. Cabrera and Y. Ishikawa, *J. Phys. Chem. Lett.*, 2010, **18**, 2622-2627.
45. N. Ramaswamy, U. Tylus, Q. Jia and S. Mukerjee, *J. Am. Chem. Soc.*, 2013, **41**, 15443-15449.
46. J. Masa, A. Zhao, W. Xia, M. Muler and W. Schuhmann, *Electrochim. Acta*, **10**, 271-278.
47. N. R. Sahraie, U. I. Kramm, J. Steinberg, Y. Zhang, Y. Thomas, T. Reier, J.-P. Paraknowisch and P. Strasser, *Nat. commun.*, 2015, **5**, 8618.
48. Y. Zhao, K. Kamiya, K. Hashimoto and S. Nakanishi, *J. Phys. Chem. C*, 2015, **5**, 2583-2588.
49. W. Xia, R. Zou, L. An, D. Xia and S. Guo, *Energy Environ. Sci.*, 2015, **8**, 568-576.
50. W. Yang, X. Yue, X. Liu, L. Chen, J. Jia and S. Guo, *Nanoscale*, 2016, **8**, 959-964.
51. A. Bonakdarpour, M. Lefevre, R. Yang, F. Jaouen, T. Dahn, J.-P. Dodelet and J. Dahn, *Electrochem. Solid-State Lett.*, 2008, **11**, B105-B108.
52. A. Bonakdarpour, T. R. Dahn, R.T. Atanasoski, M.K. Debe and J.R. Dahn, *Electrochem. Solid-State Lett.*, 2008, **11**, B208-B211.
53. M. Inaba, H. Yamada, J. Tokunaga, A. Tasaka, *Electrochem. Solid-State Lett.*, 2004, **12**, A474-a476.
54. V. Di noto, E. Negro, S. Polizzi, K. Vezzù, L. Toniolo and G. Cavinato, *Int. J. Hydrogen Energy*, 2014, **6**, 2812-2827.
55. V. Di noto, E. Negro, S. Polizzi, P. Riello and P. Atanassov, *Int. J. Hydrogen Energy*, 2012, **12**, 185-199.
56. K. Strickland, E. Miner, Q. Jia, U. Tylus, N. Ramaswamy, W. Liang, M.-T. Sougrati, F. Jaouen and S. Mukerjee, *Nat. commun.*, 2015, **6**, 7343.
57. J. Zhu, M. Xiao, C. Liu, J. Ge, J. St-Pierre and W. Xing, *J. Mater. Chem. A*, 2015, **3**, 21451-21459.

Graphical Abstract

A Fe-N-C hybrid catalyst is successfully fabricated by a simple one-step pyrolysis bimetallic Zn/Fe-ZIFs. The introduction of iron into Zn-based ZIF-7 to form the bimetallic MOFs precursors could catalyze the in situ formation of CNTs crossed porous carbons, forming a 3D hybrid network, which exhibits excellent ORR activity and stability in both acid and alkaline conditions.

